Dynamic Promotion of the Oxygen Evolution Reaction *via* Programmable Metal Oxides

Sallye R. Gathmann[1,2], Christopher J. Bartel[2], Lars C. Grabow[1,3],
Omar A. Abdelrahman[1,3], C. Daniel Frisbie[1,2], and Paul J. Dauenhauer[1,2,*]

[1] Center for Programmable Energy Catalysis (CPEC), University of Minnesota, 421 Washington Ave. SE, Minneapolis, MN, USA 55455.

[2] University of Minnesota, Department of Chemical Engineering & Materials Science, 421 Washington Ave. SE, Minneapolis, MN, USA 55455

[3] William A. Brookshire Department of Chemical and Biomolecular Engineering and Texas Center for Superconductivity (TcSUH), University of Houston, Houston, TX, USA, 77204

* Corresponding author: hauer@umn.edu

Abstract. Hydrogen gas is a promising renewable energy storage medium when produced via water electrolysis, but this process is limited by the sluggish kinetics of the anodic oxygen evolution reaction (OER). Herein, we used a microkinetic model to investigate promoting the OER using programmable oxide catalysts (*i.e.,* forced catalyst dynamics). We found that programmable catalysts could increase current density at a fixed overpotential (100X to 600X over static rates) or reduce the overpotential required to reach a fixed current density of 10 mA cm^{-2} (45 – 140% reduction vs. static). In our kinetic parameterization, the key parameters controlling the quality of the catalytic ratchet were the O*-to-OOH* and O*-to-OH* activation barriers. Our findings indicate that programmable catalysts may be a viable strategy for accelerating the OER or enabling lower-overpotential operation, but a more accurate kinetic parameterization is required for precise predictions of performance, ratchet quality, and resulting energy efficiency.

Development of carbon-neutral energy sources and energy storage mechanisms is the major challenge of the 21st century required to address climate change. Hydrogen gas is a promising energy storage medium when produced *via* water electrolysis to store renewable energy in the form of stable chemical bonds.[1,2] However, water electrolysis is not yet cost-competitive with fossil-derived H_2.[3,4] One of the major contributors to the high cost of green H_2 is the slow kinetics of the anodic oxygen evolution reaction (OER), which transforms water into $O_{2(g)}$ *via* a four electron transfer.[1,2] Slow kinetics require large overpotentials to achieve industrially relevant current densities ($\eta > 0.5$ V at 0.3 – 10 A cm^{-2}),[1] and state of the art catalysts are comprised of rare and expensive precious metal oxides such as IrO_2.[4,5]

Despite intensive research efforts over the past two decades, the intrinsic activity of OER catalysts has only modestly improved.[2,6] Activities are limited by linear free energy relationships (LFERs) that couple the binding energies of OER intermediates (*i.e.,* O*, OH*, and OOH*) on metals and oxides.[7–13] Reported for the OER by Nørskov[9,10] and Koper[14] *via* density functional theory (DFT) calculations, LFERs constrain catalyst design such that each reaction intermediate cannot be independently stabilized, preventing the design of a catalyst with thermodynamically ideal reaction energies of 1.23 eV/step.

We propose using programmable catalysts (*i.e.,* forced dynamics) as a strategy to accelerate the OER. Programmable catalysts bypass the limitations conventionally imposed by LFERs by varying the properties of a catalyst during reaction with application of an oscillating stimulus (*e.g.,* light,[15] voltage,[16–22] ferroelectric polarization,[23] *etc.*) on the time scale of a catalytic turnover.[24] Microkinetic models of programmable catalysts applied to both model reactions[25–28] and ammonia synthesis[29] have predicted that reaction rates can be increased by one or more orders of magnitude over a range of applied frequencies. Regarding the OER specifically, switchable ferroelectric polarization has been proposed as a programmable catalyst,[30,31] but no studies have analyzed the kinetics of promoting the OER *via* programmable catalysis.

In this work, programmable oxide catalysts were evaluated using a mean-field microkinetic model to assess the viability for accelerating the OER. The model is schematically represented in **Figure 1a**, and the model equations and computational methods are described in **Section S2** of the **Supporting Information** (see **Section S1** for nomenclature). The elementary steps were written based on the acidic Eley-Rideal type adsorbate evolving mechanism (AEM, **Equations S2.1-S2.4**), which features four proton-coupled electron transfer (PCET) steps.[1,9,10] This mechanism has been used in numerous OER modeling studies,[8,32–35] and there exists supporting experimental evidence.[36,37] Additionally, recent experiments excluded the meaningful participation of lattice oxygen on IrO$_2$[38] and RuO$_2$,[38,39] providing evidence against alternate mechanisms such as the lattice evolving mechanism (LOM) on those materials. However, we acknowledge that the precise mechanistic details of the OER remain debated.[36,37,40–43]

For this kinetic study, a continuum descriptor space was needed to model and optimize a generic (*i.e.,* unspecified external stimulus) programmable OER catalyst. However, parameters for both thermodynamic and kinetic scaling relations are currently unknown for this system. Periodic trends of monometallic oxides[9] were thus used as a first approximation of the thermodynamic scaling behavior of programmable OER catalysts. Following convention, the reaction free energy of step 2 at zero applied potential (ΔG_2^{0V}) was used as the catalyst descriptor.[2,44] We acknowledge that it is likely that programmable catalysts will feature scaling parameters distinct from those of periodic trends, because methods of implementing programmable catalysts change a property of the catalyst rather than the material itself. For example, programmable catalysts based on semiconductor devices tune the electron density, not nuclear composition, of metal,[16–18] oxide,[19–21] and transition metal dichalcogenide[22,45] catalysts. However, the results presented herein provide insights into the design of programmable OER catalysts and motivation for future analyses that will further refine their precise behaviors.

To parameterize the activation barriers of the OER elementary steps, we adopted the strategy used by Nørskov[46] and Mavrikakis[47] in which all PCET reactions were assumed to have the same reversible activation barrier (E_a^{eq}, see **Figure 1b**), independent of catalyst material; the catalyst identity was incorporated into the reaction kinetics through the elementary reversible potential. This strategy was utilized, because there is no widely-accepted method for calculating electrochemical activation barriers;[48,49] kinetic information also cannot be simply extracted from Tafel slopes for the OER.[5,50–52] This leads to large variation in reported activation barriers (**Figure S3.1**) and scant Brønsted-Evans-Polanyi relations for the OER.[53,54] Therefore, E_a^{eq} was treated as an adjustable model parameter and varied between 0.16 and 0.66 eV; these bounds were approximated from a literature review of calculated kinetic barriers for the OER on oxide catalysts (details, **SI section S3**).[53,55–62] The kinetics of the OER were then evaluated using the Butler-Volmer framework,[63,64] and the microkinetic model was solved at differential conversion conditions at pH = 0 in Julia.[65,66] Mass transport effects were not considered.

To assess the values of the reversible activation barrier (E_a^{eq}) used in the model, simulations were conducted at static (*i.e.,* non-oscillating) conditions to determine the minimum overpotential ($\eta_{i=10}$) required to reach a current density of 10 mA cm^{-2}, a common benchmark value.[67] **Figure 1c** depicts these simulated overpotential volcanoes. Markers overlaid on the volcano plot compare both theoretical (black)[9] and experimental (pink)[68–72] overpotentials for various oxide catalysts (see **Figure S4.1** for a magnified view near the volcano peak). Models with E_a^{eq} between 0.26 and 0.46 eV returned peak overpotentials ($\eta_{i=10}^{peak}$) of 229 – 451 mV (**Table S4.1**), which is in the range of experimentally-measured overpotentials of highly active OER catalysts in highly acidic electrolyte at this current density (*e.g.,* 220 – 260 mV for RuO$_x$,[68,69] 373 – 458 mV for IrO$_x$,[68–70] and 468 mV for CoO$_x$;[71] see **Table S4.2**). These E_a^{eq} values are also within the range of DFT calculations for AEM steps 3 and 4 on IrO$_2$ (0.36 – 0.54 eV and ~0.4 – 0.5 eV, respectively),[57,59,62] but lower than reported for step 3 on RuO$_2$ (~0.6 eV).[56] In our model, E_a^{eq} of 0.56 – 0.66 eV returned peaks between 645 and 845 mV, far larger than experimental values; at E_a^{eq} of 0.16 eV, the model underpredicted both theoretical and experimental overpotentials.

Gathmann, et al.

During reaction, a programmable catalyst will be held at a constant working electrode potential (*i.e.,* constant overpotential); the application of an *additional* stimulus oscillates the properties of the catalyst and thus surface energetics. This additional stimulus can be a voltage applied to a catalytic condenser[16–19] or transistor,[20–22,45] strain,[29] ferroelectric polarization,[23,30,31] *etc.*; this mechanism is not specified in our model. To generate a performance baseline, we simulated OER current density volcanoes at a constant overpotential for an intermediate E_a^{eq} value of 0.46 eV, which featured close agreement between model and experimental $\eta_{i=10}^{peak}$; the results are shown in **Figure 2**. Each current density volcano has several distinct regions (**Figure 2a**): to the left of the peak, step 3 (OOH* formation) was the potential determining step (PDS) for all simulated overpotentials (see *e.g.,* **Figure 2f**) and the surface is covered by O* (**Figure 2d**). To the right of the peak, the PDS was step 2 (O* formation) (see *e.g.,* **Figure 2g**) and the dominant coverage transitioned from O* to OH* to empty sites as ΔG_2^{0V} increased (**Figures 2c & 2b**). Step 4 (O$_{2(g)}$ formation) was essentially barrierless at $\eta > 0$ V across most of the descriptor space, so there was never any appreciable coverage of OOH* (**Figure 2e**). A degree of rate control analysis (**Figure S4.4**) revealed that the rate-determining step (RDS) at the high-ΔG_2^{0V} side of the volcano was step 2; to the immediate left of the peak, the RDS switched to step 3. While only steps 2 and 3 are considered relevant from a purely thermodynamic viewpoint,[9] recent studies considering kinetic barriers have proposed that O$_2$ formation can be rate limiting on IrO$_2$[40,41,73] and RuO$_2$.[74,75] Our model predicted $X_{RC,4} \sim 1$ at $\Delta G_2^{0V} \lesssim 1$ eV, which is lower than the DFT-calculated[9] ΔG_2^{0V} of IrO$_2$ (1.3 – 1.5 eV) and RuO$_2$ (1.47 – 1.49 eV). Similar trends were observed for constant-potential simulations at other E_a^{eq} values (**Figures S4.5 – S4.9**).

Programmable catalysts were simulated by defining two states between which the catalyst oscillated according to a square waveform with tunable frequency (f), amplitude ($\Delta\Delta G_2$), center point (ΔG_2^{ctr}), and duty cycle (ϕ, fractional time at state 1). All waveform parameters were defined with respect to the zero applied potential reaction coordinate. One set of rate constants was calculated for each catalyst state, and the programmable catalyst was modeled by switching the rate constants at the specified time points (determined by the waveform frequency and duty cycle) during ODE integration using callbacks in Julia (details, **SI Section S2**).[65,66] After the model reached a dynamic steady state (*i.e.,* limit cycle), the time-averaged OER current density was calculated by averaging over five oscillations.
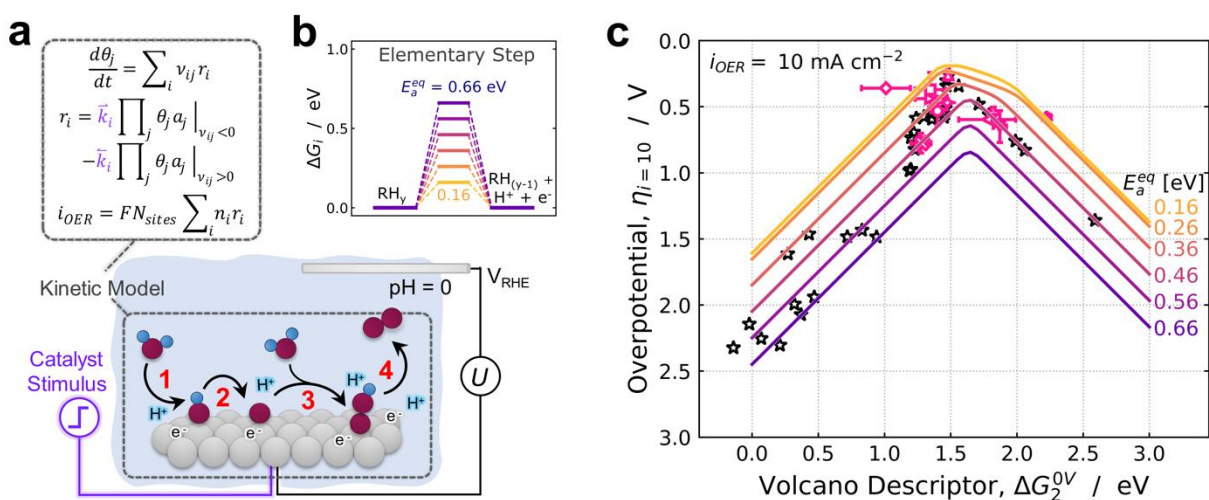

Figure 1. Microkinetic model description. **(a)** Schematic representation of our microkinetic model of the OER. Inset **(b)** illustrates the definition of E_a^{eq}. **(c)** OER overpotential volcano at a current density of $i_{OER} = 10$ mA cm^{-2}. Solid lines show microkinetic model results as a function of the reversible activation barrier ($E_a^{eq} \in [0.16, 0.66]$ eV); black ☆[9] are theoretical overpotentials predicted *via* DFT; pink markers[67–71] are experimentally measured overpotentials in acidic electrolyte (details, *Table S4.2*).

We note that oscillation of a working electrode potential has been experimentally demonstrated to accelerate formic acid electro-oxidation rates 20–30×,[76,77] improve the Faradaic efficiency of CO_2 electrolysis,[78,79] and even increase the rate of ethylene hydrogenation (which is not promoted by static potentials) by ~550%.[80] However, it should be emphasized that *oscillating the electrode potential is conceptually distinct from the type of programmable catalyst modeled in this study*.[28] When a potential is oscillated to a higher value, all (electrochemical) steps proceed with larger thermodynamic driving force and lower activation energies (see *e.g.,* the purple → blue reaction coordinates in **Figure 2f**, which show the effect of increasing η from 0 to 500 mV). Conversely,

application of an oscillating stimulus to a programmable catalyst modifies the energetics of adsorbates via a change in electron density. In our model, this is represented by oscillating the catalyst descriptor at constant potential (*i.e.,* at a fixed electrochemical driving force); this makes some steps more energetically favorable, and others less so (compare reaction coordinates in **Figures 2f & 2g** at $U = 0$ V; the PDS switches from step 3 to step 2, respectively). It is this biasing of the reaction coordinate from one state to another that is responsible for the orders-of-magnitude rate enhancement observed in previous modeling studies.[25–28]
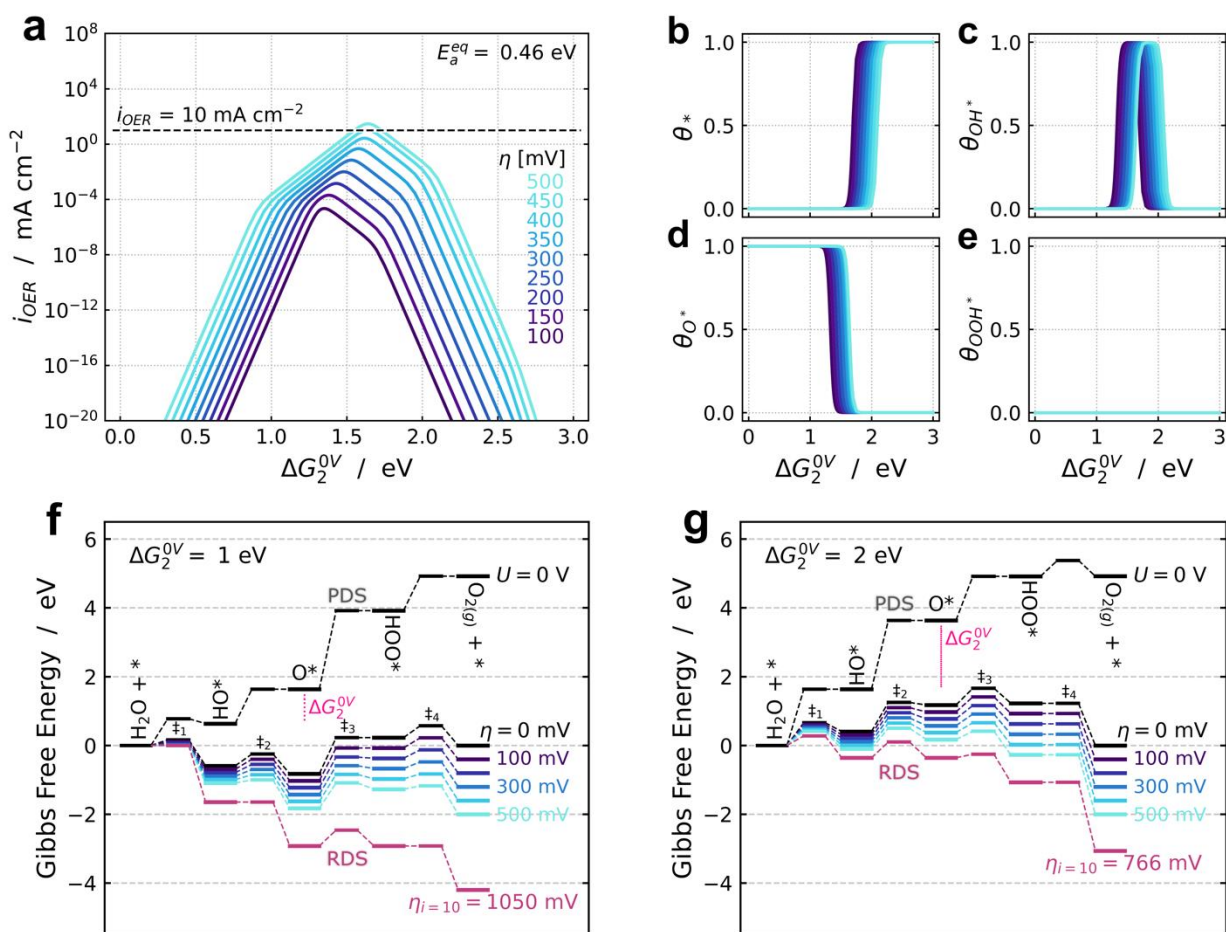

Figure 2. Static OER simulation results. **(a)** OER current density volcano and **(b-e)** surface coverages for $E_a^{eq} = 0.46$ eV at overpotentials $\eta \in [100, 500]$ mV. **(f-g)** Reaction coordinates at $E_a^{eq} = 0.46$ eV as a function of the electrochemical potential at $\Delta G_2^{0V} = 1$ eV and 2 eV, respectively. The black line shows the reaction coordinate at zero applied potential; purple → blue lines correspond to the constant-potential simulation results (panels a-e); and pink to the overpotential volcano (Figure 1c), depicting the reaction coordinate at the minimum overpotential ($\eta_{i=10}$) required to reach $i_{OER} = 10$ mA cm^{-2}.

Figure 3 depicts three examples of programmable catalyst simulations for an intermediate reversible activation barrier (E_a^{eq}) of 0.46 eV, with fixed waveform parameters (center point $\Delta G_2^{ctr} = 1.5$ eV, amplitude $\Delta\Delta G_2 = 1$ eV, frequency $f = 1$ kHz, and duty cycle $\phi = 50\%$). **Figures 3a-3d** show the results of a simulation at $\eta = 650$ mV, which yields an effective state 2 *forward* ratchet for O* (*i.e.,* O* prefers to react

forwards to OOH* rather than backwards to OH*). The dominant reaction pathway of surface molecules is shown in **Figure 3a** as the catalyst oscillated between the two states. In state 1 (navy), water dissociates to form OH* and then O*, which covers the surface (**Figure 3b**) because it cannot react further due to the large barrier of step 3. Upon switching the catalyst to state 2 (grey), the majority of surface O* followed the more kinetically facile
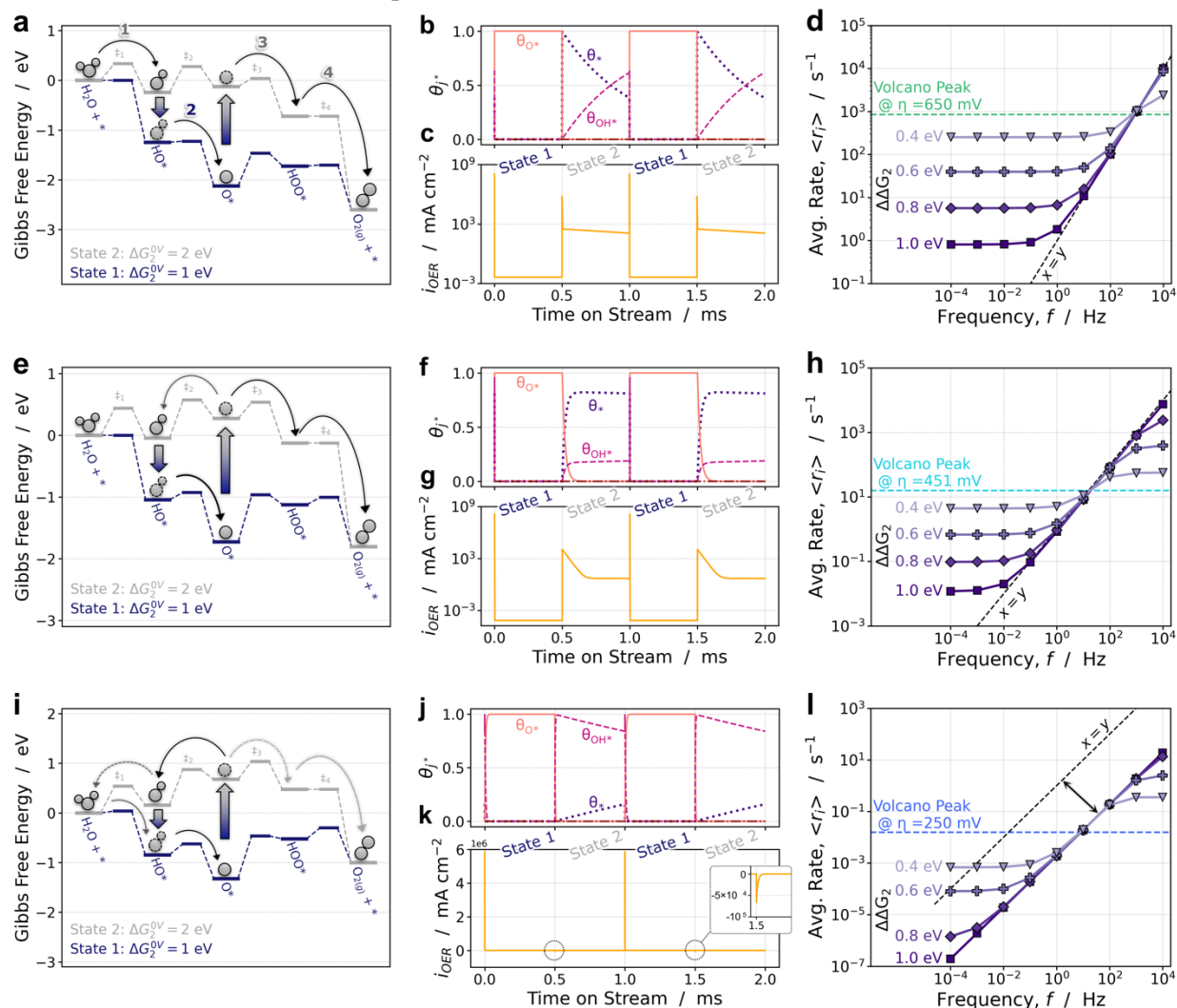

Figure 3. Selected programmable catalyst simulations for $E_a^{eq} = 0.46$ eV at different overpotentials corresponding to different quality ratchets. All panels have the same waveform parameters (center point $\Delta G_2^{ctr} = 1.5$ eV, duty cycle $\phi = 50\%$, amplitude $\Delta\Delta G_2 = 1$ eV, and frequency $f = 1$ kHz). **(a)** Reaction coordinate of an 'effective' forward ratchet at $\eta = 650$ mV; **(b,c)** time on stream data for surface coverages and current density; **(d)** frequency response plot. The frequency response traces overlap the parity line, indicating there is ~1 catalytic turnover per catalyst oscillation, corresponding to an efficient ratchet. **(e)** Reaction coordinate of an 'intermediate' ratchet at $\eta = \eta_{i=10}^{peak}$ (451 mV); **(f,g)** time on stream data for surface coverages and current density; **(h)** frequency response plot. **(i)** Reaction coordinate of a 'reverse' ratchet at $\eta = 250$ mV; **(j,k)** time on stream data for surface coverages and current density; **(l)** frequency response plot where traces are far from the parity line, indicating an inefficient programmable catalyst.

pathway to produce $O_{2(g)}$; this created open sites on the catalyst surface, which were slowly populated with OH* (**Figure 3b**). Upon switching back to state 1, the OH* and any remaining empty sites were rapidly converted to O*, completing the catalytic cycle. The relative rates of surface coverage changes were determined by the forward activation barriers (**Figure 3a**); formation of O* is barrierless in catalyst state 1, while formation of both OH* and OOH* in state 2 have small barriers (0.34 and 0.16 eV, respectively). Rapid change in surface coverages was also apparent in the magnitude of the current density spikes that occurred when switching catalyst states (**Figure 3c**), with the switch from state 2 to state 1 (barrierless O* formation) featuring the larger spike due to the faster catalytic rate.

The example of **Figures 3a-3d** is characterized as an 'effective' forward ratchet due to small forward activation barriers and simultaneously large backward activation barriers. For every catalyst cycle between states ($1 \rightarrow 2 \rightarrow 1$), each site predominately yields one turnover to form $O_{2(g)}$. This is apparent in the frequency response plot of **Figure 3d**, which shows the time-averaged catalytic rates (s^{-1}) relative to applied waveform frequency (Hz [=] s^{-1}) at oscillation amplitudes ($\Delta\Delta G_2$) between 0.4 and 1.0 eV. At $\Delta\Delta G_2 > 0.4$ eV, each trace overlaps with the parity line (y = x), indicating an efficient dynamic catalyst of one catalytic turnover per oscillation.

Figures 3e-3h depict an intermediate quality catalytic ratchet in state 2 (grey), which results from a simulation at $\eta = 451$ mV ($\eta_{i=10}^{peak}$ for E_a^{eq} of 0.46 eV). As shown in **Figure 3e**, the forward barrier for O*-to-OOH* formation in state 2 (grey) is only slightly smaller than the reverse barrier of O*-to-OH* formation (0.26 vs. 0.3 eV, respectively). Thus, as the catalyst switches from state 1 to state 2, a small fraction of the O* reacts backwards to form OH* instead of following the forward pathway to produce $O_{2(g)}$ (**Figure 3f & 3g**). However, the majority of molecules still proceed forward such that frequency response traces (**Figure 3h**) are comparable to the parity line, indicating that one catalyst oscillation ($1 \rightarrow 2 \rightarrow 1$) still yields about one catalytic turnover.

The third example in **Figures 3i-3l** depicts a *reverse* O* ratchet in state 2 for a simulation conducted at $\eta = 250$ mV. Consistent with the prior two examples, the catalyst surface is covered in O* in state 1 (**Figure 3j**). However, as depicted in **Figure 3i**, the kinetically favorable reaction pathway for O* in state 2 is the *reverse* reaction pathway from O* to OH* (0.2 eV barrier, vs. 0.36 eV for O* to OOH*). When the catalyst switches from state 1 to state 2, the surface coverage of OH* immediately increases to ~1 (**Figure 3j**); after forming OH*, the molecules continue along the reverse reaction pathway to produce empty sites. Because most molecules are following the reverse reaction pathway, the current density is negative in state 2 (**Figure 3k**). For this programmable catalyst, only a small fraction of O* molecules react to OOH* and follow the forward pathway to $O_{2(g)}$. This inefficiency is apparent in the frequency response plot (**Figure 3l**), as the average catalytic rate traces are now far from the parity line. Despite this catalytic inefficiency, the programmable catalyst still achieves ~1,200× higher rates than the corresponding volcano peak when oscillated at sufficiently fast rates.

Programmable catalysts were then simulated with different waveform parameters to maximize OER activity. Simulations were conducted at both $\eta_{i=10}^{peak}$, corresponding to an intermediate quality ratchet (*e.g.,* **Figures 3e-3h**), and at the minimum overpotential ($\eta_{i=10}$) required to reach 10 mA cm^{-2}, which typically corresponded to a 'reverse O*' ratchet (*e.g.,* **Figures 3i-3l**). The key results from these simulations at an intermediate reversible activation barrier (E_a^{eq}) of 0.46 eV are shown in **Figures 4a-4c**. **Figure 4a** compares static (dashed lines) and programmable (markers) catalyst performance at overpotentials (η) of 250 mV and 451 mV ($\eta_{i=10}^{peak}$) for a 50% duty cycle waveform with amplitude $\Delta\Delta G_2 = 0.5$ eV and frequency $f = 10$ kHz. At both η values, the programmable catalyst achieved ~60× higher current densities than the respective static volcano maximum. The heatmap of **Figure 4b** shows the results of simulations at the larger overpotential (451 mV, $\eta_{i=10}^{peak}$) where the amplitude ($\Delta\Delta G_2$) was varied between 0.1 and 1.0 eV; static results are depicted at $\Delta\Delta G_2 = 0$ eV. As $\Delta\Delta G_2$ increased, the current density also increased, as expected. The maximum current density achieved by this programmable catalyst was ~5,300 mA cm^{-2} at $\Delta\Delta G_2 = 1.0$ eV, corresponding to a ~520× increase over the static volcano peak.

Gathmann, et al.   **Page 6**

Next, the ability of programmable catalysts to decrease overpotential was assessed by setting a target current density of 10 mA cm^{-2} and simulating the minimum overpotential ($\eta_{i=10}$) required to reach this target in 50 mV increments. The heatmap of **Figure 4c** shows the results at a reversible activation barrier (E_a^{eq}) of 0.46 eV as a function of waveform center point (ΔG_2^{ctr}) and amplitude ($\Delta\Delta G_2$) for a 50% duty cycle waveform oscillating at 10 kHz frequency; static results are again shown

at $\Delta\Delta G_2 = 0$ eV. A minimum $\Delta\Delta G_2$ of 0.3 eV was necessary to outperform the static volcano peak ($\eta_{i=10}^{peak} = 451$ mV). Increasing $\Delta\Delta G_2$ to 0.4 eV further decreased $\eta_{i=10}$ to 350 mV, and at $\Delta\Delta G_2$ of 0.9 eV or higher, a minimum $\eta_{i=10}$ of 250 mV was achieved, corresponding to a 45% decrease from the static $\eta_{i=10}^{peak}$. Tuning the waveform duty cycle (ϕ) allowed a larger range of ΔG_2^{ctr} to reach the

Figure 4. Programmable OER simulation results. Unless noted otherwise, results are shown for $E_a^{eq} = 0.46$ eV with waveform parameters duty cycle $\phi = 50\%$ and frequency $f = 10$ kHz. **(a)** Comparison of static (dashed lines) and programmable (markers) OER catalysts at overpotentials η of 250 and 451 mV with waveform amplitude $\Delta\Delta G_2 = 0.5$ eV. At both η values shown, the programmable catalyst achieves current densities $\sim 60 \times$ above the corresponding volcano peak. **(b)** Heatmap showing the current density achieved by a programmable catalyst operating at $\eta_{i=10}^{peak}$ (451 mV) as a function of waveform center point and amplitude. $\Delta\Delta G_2 = 0$ eV represents static results. **(c)** Heatmap showing the minimum overpotential ($\eta_{i=10}$) needed to achieve $i_{OER} = 10$ mA cm^{-2} as a function of waveform center point and amplitude. $\Delta\Delta G_2 = 0$ eV represents static results (see *Figure 1c*). **(d)** Maximum current density achieved by optimized programmable catalysts operating at $\eta_{i=10}^{peak}$ as a function of the reversible activation barrier E_a^{eq} (see *Table S5.1* for corresponding waveform parameters). Numbers represent the enhancement over the static volcano peak. **(e)** Reduction in $\eta_{i=10}$ by programmable catalysts as a function of the reversible activation barrier E_a^{eq}. Static values correspond to volcano peaks of *Figure 1c*, and programmable values to optimized waveforms (see *Table S5.2* for corresponding waveform parameters).

target current density at the minimum $\eta_{i=10}$ of 250 mV (details, **SI Section S5.2**).

Figures **4d-4e** show how the reversible activation barrier (E_a^{eq}) value impacts the simulated performance of programmable catalysts. **Figure 4d** compares the maximum current densities achieved by optimized programmable catalysts within the bounds of sampled parameters (see **Table S5.1** for optimized waveform parameters) operating at the respective static volcano peak overpotentials ($\eta_{i=10}^{peak}$, **Table S4.1**). For E_a^{eq} of $0.16 - 0.26$ eV, ~300× enhancement was achieved, correspond to current densities ~ 3,200 mA cm^{-2}. E_a^{eq} of 0.36 eV returned the lowest performance at only 110× enhancement (1,100 mA cm^{-2}), and E_a^{eq} of $0.56 - 0.66$ eV both achieved 620× enhancement (~ 6,400 mA cm^{-2}). For E_a^{eq} of 0.46 eV and larger, $\eta_{i=10}^{peak}$ results in 'effective' forward ratchets with relevant forward barriers of ~0.2 eV (**Figures S5.4d & S5.5d**). This leads to these systems experiencing close to maximal performance at the maximum oscillation frequency sampled (*i.e.,* resonance frequencies on the order of 10 kHz, **Figures S5.4b & S5.5b**). For $E_a^{eq} \leq 0.26$ eV, ratchets are of 'intermediate' quality (**Figure S5.1d & S5.2d**). However, barriers are almost nonexistent, resulting in resonance frequencies far above 10 kHz (**Figures S5.1b & S5.2b**). For E_a^{eq} of 0.36 eV, which returned the lowest rate enhancement, the ratchet is a mild 'reverse' ratchet (**Figure S5.3d**) and resonance frequencies are above 10 kHz (**Figure S5.3b**); this combination hinders rate enhancement.

Figure **4e** compares overpotential-optimized programmable catalysts (see **Table S5.2** for optimized waveform parameters) with the highest-performing static catalysts (*e.g.,* peak overpotentials $\eta_{i=10}^{peak}$ of **Figure 1c**). For the most physically-representative reversible activation barrier values sampled in this model (E_a^{eq} of $0.26 - 0.46$ eV), $\eta_{i=10}$ of programmable catalysts was $30 - 250$ mV (compare to $\eta_{i=10}^{peak}$ of $229 - 451$ mV). At the larger end of E_a^{eq} values simulated, reductions of ~50% were achieved, corresponding to $\eta_{i=10}$ values of 300 and 410 mV for E_a^{eq} of 0.56 eV and 0.66 eV, respectively. For E_a^{eq} of 0.16 eV, the optimized programmable catalyst resulted in $\eta_{i=10}$ of -70 mV. While this may seem like an error in the kinetic model, previous simulations have demonstrated that programmable catalysts can drive reactions away from equilibrium because they impart work directly into the surface reaction by changing the energetics of intermediates with time.[26,27,29,81] This phenomena of a fluctuating energy source driving reactions away from equilibrium is also well-documented in the molecular machines community.[82–84]

In this work, microkinetic simulations of programmable OER catalysts were conducted using a simple kinetic parameterization in which all proton-coupled electron transfer (PCET) reaction steps featured the same reversible activation barrier (E_a^{eq}), which was varied between $0.16 - 0.66$ eV. We found that volcano peak overpotentials ($\eta_{i=10}$) predicted by our model at intermediate values of E_a^{eq} ($0.26 - 0.46$ eV) featured closest agreement with literature. For this range of E_a^{eq} values, programmable catalyst simulations conducted at the volcano peak overpotential(s) achieved current densities ~100 – 500× higher than static, while programmable catalysts simulated at a benchmark current density of 10 mA cm^{-2} were able to operate at 45 – 90% lower overpotentials than static. Additionally, we found that this kinetic parameterization led to 'effective' forward ratchets at high overpotentials, while the ratchets became less effective (even promoting backwards reaction) at low overpotentials. The key parameters controlling ratchet quality were the O*-to-OOH* and O*-to-OH* formation barriers at the high ΔG_2^{0V} catalyst state.

This simple kinetic model demonstrated that programmable catalysts are a potentially viable strategy to accelerate the OER and/or reduce the overpotential required to reach a specific current density. By accelerating the OER, programmable catalysts may enable the use of cheaper, more abundant catalyst materials. However, future work improving the parameterization of OER kinetics by replacing the assumed LFERs and single-valued reversible activation barrier is required to enable more accurate predictions of rate enhancement and ratchet quality for the programmable OER. This is requisite for determining the energy efficiency of programmable OER catalysts.

Keywords. Hydrogen, electrolysis, dynamics, programmable, resonance

Supporting Information. List of variables; complete microkinetic model equations and computational methods; brief literature review of kinetic scaling relations and barriers reported for the OER; method for estimating bounds of the reversible activation barrier; additional static catalyst simulation results; additional programmable catalyst simulation results; additional references [85–117].

References

(1) Chatenet, M.; Pollet, B. G.; Dekel, D. R.; Dionigi, F.; Deseure, J.; Millet, P.; Braatz, R. D.; Bazant, M. Z.; Eikerling, M.; Staffell, I.; Balcombe, P.; Shao-Horn, Y.; Schäfer, H. Water Electrolysis: From Textbook Knowledge to the Latest Scientific Strategies and Industrial Developments. *Chem. Soc. Rev.* **2022**, *51* (11), 4583–4762. https://doi.org/10.1039/D0CS01079K.

(2) Seh, Z. W.; Kibsgaard, J.; Dickens, C. F.; Chorkendorff, I.; Nørskov, J. K.; Jaramillo, T. F. Combining Theory and Experiment in Electrocatalysis: Insights into Materials Design. *Science* **2017**, *355* (6321), eaad4998. https://doi.org/10.1126/science.aad4998.

(3) Nnabuife, S. G.; Ugbeh-Johnson, J.; Okeke, N. E.; Ogbonnaya, C. Present and Projected Developments in Hydrogen Production: A Technological Review*. *Carbon Capture Science & Technology* **2022**, *3*, 100042. https://doi.org/10.1016/j.ccst.2022.100042.

(4) Terlouw, T.; Bauer, C.; McKenna, R.; Mazzotti, M. Large-Scale Hydrogen Production *via* Water Electrolysis: A Techno-Economic and Environmental Assessment. *Energy Environ. Sci.* **2022**, *15* (9), 3583–3602. https://doi.org/10.1039/D2EE01023B.

(5) Shih, A. J.; Monteiro, M. C. O.; Dattila, F.; Pavesi, D.; Philips, M.; Da Silva, A. H. M.; Vos, R. E.; Ojha, K.; Park, S.; Van Der Heijden, O.; Marcandalli, G.; Goyal, A.; Villalba, M.; Chen, X.; Gunasooriya, G. T. K. K.; McCrum, I.; Mom, R.; López, N.; Koper, M. T. M. Water Electrolysis. *Nat Rev Methods Primers* **2022**, *2* (1), 84. https://doi.org/10.1038/s43586-022-00164-0.

(6) Govindarajan, N.; Kastlunger, G.; Heenen, H. H.; Chan, K. Improving the Intrinsic Activity of Electrocatalysts for Sustainable Energy Conversion: Where Are We and Where Can We Go? *Chem. Sci.* **2022**, *13* (1), 14–26. https://doi.org/10.1039/D1SC04775B.

(7) Gunasooriya, G. T. K. K.; Nørskov, J. K. Analysis of Acid-Stable and Active Oxides for the Oxygen Evolution Reaction. *ACS Energy Lett.* **2020**, *5* (12), 3778–3787. https://doi.org/10.1021/acsenergylett.0c02030.

(8) Zhang, J.; Tao, H. B.; Kuang, M.; Yang, H. B.; Cai, W.; Yan, Q.; Mao, Q.; Liu, B. Advances in Thermodynamic-Kinetic Model for Analyzing the Oxygen Evolution Reaction. *ACS Catal.* **2020**, *10* (15), 8597–8610. https://doi.org/10.1021/acscatal.0c01906.

(9) Man, I. C.; Su, H.; Calle-Vallejo, F.; Hansen, H. A.; Martínez, J. I.; Inoglu, N. G.; Kitchin, J.; Jaramillo, T. F.; Nørskov, J. K.; Rossmeisl, J. Universality in Oxygen Evolution Electrocatalysis on Oxide Surfaces. *ChemCatChem* **2011**, *3* (7), 1159–1165. https://doi.org/10.1002/cctc.201000397.

(10) Rossmeisl, J.; Qu, Z.-W.; Zhu, H.; Kroes, G.-J.; Nørskov, J. K. Electrolysis of Water on Oxide Surfaces. *Journal of Electroanalytical Chemistry* **2007**, *607* (1–2), 83–89. https://doi.org/10.1016/j.jelechem.2006.11.008.

(11) Divanis, S.; Kutlusoy, T.; Ingmer Boye, I. M.; Man, I. C.; Rossmeisl, J. Oxygen Evolution Reaction: A Perspective on a Decade of Atomic Scale Simulations. *Chem. Sci.* **2020**, *11* (11), 2943–2950. https://doi.org/10.1039/C9SC05897D.

(12) Koper, M. T. M. Theory of Multiple Proton–Electron Transfer Reactions and Its Implications for Electrocatalysis. *Chem. Sci.* **2013**, *4* (7), 2710. https://doi.org/10.1039/c3sc50205h.

(13) Guo, C.; Fu, X.; Xiao, J. Theoretical Insights on the Synergy and Competition between Thermochemical and Electrochemical Steps in Oxygen Electroreduction. *J. Phys. Chem. C* **2020**, *124* (47), 25796–25804. https://doi.org/10.1021/acs.jpcc.0c06691.

(14) Koper, M. T. M. Thermodynamic Theory of Multi-Electron Transfer Reactions: Implications for

Electrocatalysis. *Journal of Electroanalytical Chemistry* **2011**, *660* (2), 254–260. https://doi.org/10.1016/j.jelechem.2010.10.004.

(15) Qi, J.; Resasco, J.; Robatjazi, H.; Alvarez, I. B.; Abdelrahman, O.; Dauenhauer, P.; Christopher, P. Dynamic Control of Elementary Step Energetics via Pulsed Illumination Enhances Photocatalysis on Metal Nanoparticles. *ACS Energy Lett.* **2020**, *5* (11), 3518–3525. https://doi.org/10.1021/acsenergylett.0c01978.

(16) Onn, T. M.; Oh, K.-R.; Adrahtas, D. Z.; Soeherman, J. K.; Hopkins, J. A.; Frisbie, C. D.; Dauenhauer, P. J. Flexible and Extensive Platinum Ion Gel Condensers for Programmable Catalysis. *ACS Nano* **2024**, *18* (1), 983–995. https://doi.org/10.1021/acsnano.3c09815.

(17) Oh, K.-R.; Onn, T. M.; Walton, A.; Odlyzko, M. L.; Frisbie, C. D.; Dauenhauer, P. J. Fabrication of Large-Area Metal-on-Carbon Catalytic Condensers for Programmable Catalysis. *ACS Appl. Mater. Interfaces* **2024**, *16* (1), 684–694. https://doi.org/10.1021/acsami.3c14623.

(18) Onn, T. M.; Gathmann, S. R.; Guo, S.; Solanki, S. P. S.; Walton, A.; Page, B. J.; Rojas, G.; Neurock, M.; Grabow, L. C.; Mkhoyan, K. A.; Abdelrahman, O. A.; Frisbie, C. D.; Dauenhauer, P. J. Platinum Graphene Catalytic Condenser for Millisecond Programmable Metal Surfaces. *J. Am. Chem. Soc.* **2022**, *144* (48), 22113–22127. https://doi.org/10.1021/jacs.2c09481.

(19) Onn, T. M.; Gathmann, S. R.; Wang, Y.; Patel, R.; Guo, S.; Chen, H.; Soeherman, J. K.; Christopher, P.; Rojas, G.; Mkhoyan, K. A.; Neurock, M.; Abdelrahman, O. A.; Frisbie, C. D.; Dauenhauer, P. J. Alumina Graphene Catalytic Condenser for Programmable Solid Acids. *JACS Au* **2022**, *2* (5), 1123–1133. https://doi.org/10.1021/jacsau.2c00114.

(20) Kim, C.-H.; Wang, Y.; Frisbie, C. D. Continuous and Reversible Tuning of Electrochemical Reaction Kinetics on Back-Gated 2D Semiconductor Electrodes: Steady-State Analysis Using a Hydrodynamic Method. *Anal. Chem.* **2019**, *91* (2), 1627–1635. https://doi.org/10.1021/acs.analchem.8b05216.

(21) Wang, Y.; Wang, Y.; Frisbie, C. D. Electrochemistry at Back-Gated, Ultrathin ZnO Electrodes: Field-Effect Modulation of Heterogeneous Electron Transfer Rate Constants by 30× with Enhanced Gate Capacitance. *ACS Appl. Mater. Interfaces* **2023**.

(22) Wang, Y.; Udyavara, S.; Neurock, M.; Frisbie, C. D. Field Effect Modulation of Electrocatalytic Hydrogen Evolution at Back-Gated Two-Dimensional MoS$_2$ Electrodes. *Nano Lett.* **2019**, *19* (9), 6118–6123. https://doi.org/10.1021/acs.nanolett.9b02079.

(23) Jung, S.; Pizzolitto, C.; Biasi, P.; Dauenhauer, P. J.; Birol, T. Programmable Catalysis by Support Polarization: Elucidating and Breaking Scaling Relations. *Nat Commun* **2023**, *14* (1), 7795. https://doi.org/10.1038/s41467-023-43641-0.

(24) Shetty, M.; Walton, A.; Gathmann, S. R.; Ardagh, M. A.; Gopeesingh, J.; Resasco, J.; Birol, T.; Zhang, Q.; Tsapatsis, M.; Vlachos, D. G.; Christopher, P.; Frisbie, C. D.; Abdelrahman, O. A.; Dauenhauer, P. J. The Catalytic Mechanics of Dynamic Surfaces: Stimulating Methods for Promoting Catalytic Resonance. *ACS Catal.* **2020**, *10* (21), 12666–12695. https://doi.org/10.1021/acscatal.0c03336.

(25) Ardagh, M. A.; Abdelrahman, O. A.; Dauenhauer, P. J. Principles of Dynamic Heterogeneous Catalysis: Surface Resonance and Turnover Frequency Response. *ACS Catal.* **2019**, *9* (8), 6929–6937. https://doi.org/10.1021/acscatal.9b01606.

(26) Ardagh, M. A.; Birol, T.; Zhang, Q.; Abdelrahman, O. A.; Dauenhauer, P. J. Catalytic Resonance Theory: superVolcanoes, Catalytic Molecular Pumps, and Oscillatory Steady State. *Catal. Sci. Technol.* **2019**, *9* (18), 5058–5076. https://doi.org/10.1039/C9CY01543D.

(27) Gathmann, S. R.; Ardagh, M. A.; Dauenhauer, P. J. Catalytic Resonance Theory: Negative Dynamic Surfaces for Programmable Catalysts. *Chem Catalysis* **2022**, *2* (1), 140–163. https://doi.org/10.1016/j.checat.2021.12.006.

(28) Baz, A.; Lyons, M.; Holewinski, A. Dynamic Electrocatalysis: Examining Resonant Catalytic Rate Enhancement under Oscillating Electrochemical Potential. *Chem Catalysis* **2022**, *2* (12), 3497–3516. https://doi.org/10.1016/j.checat.2022.09.002.

(29) Wittreich, G. R.; Liu, S.; Dauenhauer, P. J.; Vlachos, D. G. Catalytic Resonance of Ammonia Synthesis by Simulated Dynamic Ruthenium Crystal Strain. *Sci. Adv.* **2022**, *8* (4), eabl6576. https://doi.org/10.1126/sciadv.abl6576.

(30) Lan, Z.; Småbråten, D. R.; Xiao, C.; Vegge, T.; Aschauer, U.; Castelli, I. E. Enhancing Oxygen Evolution Reaction Activity by Using Switchable Polarization in Ferroelectric InSnO$_2$N. *ACS Catal.* **2021**, *11* (20), 12692–12700. https://doi.org/10.1021/acscatal.1c03737.

(31) Spezzati, C.; Lan, Z.; Castelli, I. E. Dynamic Strain

and Switchable Polarization: A Pathway to Enhance the Oxygen Evolution Reaction on InSnO2N. *Journal of Catalysis* **2022**, *413*, 720–727. https://doi.org/10.1016/j.jcat.2022.07.021.

(32) Fornaciari, J. C.; Weng, L.-C.; Alia, S. M.; Zhan, C.; Pham, T. A.; Bell, A. T.; Ogitsu, T.; Danilovic, N.; Weber, A. Z. Mechanistic Understanding of pH Effects on the Oxygen Evolution Reaction. *Electrochimica Acta* **2022**, *405*, 139810. https://doi.org/10.1016/j.electacta.2021.139810.

(33) Huang, J.; Li, M.; Eslamibidgoli, M. J.; Eikerling, M.; Groß, A. Cation Overcrowding Effect on the Oxygen Evolution Reaction. *JACS Au* **2021**, *1* (10), 1752–1765. https://doi.org/10.1021/jacsau.1c00315.

(34) Nishimoto, T.; Shinagawa, T.; Naito, T.; Takanabe, K. Microkinetic Assessment of Electrocatalytic Oxygen Evolution Reaction over Iridium Oxide in Unbuffered Conditions. *Journal of Catalysis* **2020**, *391*, 435–445. https://doi.org/10.1016/j.jcat.2020.09.007.

(35) Mefford, J. T.; Zhao, Z.; Bajdich, M.; Chueh, W. C. Interpreting Tafel Behavior of Consecutive Electrochemical Reactions through Combined Thermodynamic and Steady State Microkinetic Approaches. *Energy Environ. Sci.* **2020**, *13* (2), 622–634. https://doi.org/10.1039/C9EE02697E.

(36) Naito, T.; Shinagawa, T.; Nishimoto, T.; Takanabe, K. Recent Advances in Understanding Oxygen Evolution Reaction Mechanisms over Iridium Oxide. *Inorg. Chem. Front.* **2021**, *8* (11), 2900–2917. https://doi.org/10.1039/D0QI01465F.

(37) Reier, T.; Nong, H. N.; Teschner, D.; Schlögl, R.; Strasser, P. Electrocatalytic Oxygen Evolution Reaction in Acidic Environments - Reaction Mechanisms and Catalysts. *Adv. Energy Mater.* **2017**, *7* (1), 1601275. https://doi.org/10.1002/aenm.201601275.

(38) Scott, S. B.; Sørensen, J. E.; Rao, R. R.; Moon, C.; Kibsgaard, J.; Shao-Horn, Y.; Chorkendorff, I. The Low Overpotential Regime of Acidic Water Oxidation Part II: Trends in Metal and Oxygen Stability Numbers. *Energy Environ. Sci.* **2022**, *15* (5), 1988–2001. https://doi.org/10.1039/D1EE03915F.

(39) Stoerzinger, K. A.; Diaz-Morales, O.; Kolb, M.; Rao, R. R.; Frydendal, R.; Qiao, L.; Wang, X. R.; Halck, N. B.; Rossmeisl, J.; Hansen, H. A.; Vegge, T.; Stephens, I. E. L.; Koper, M. T. M.; Shao-Horn, Y. Orientation-Dependent Oxygen Evolution on RuO$_2$ without Lattice Exchange. *ACS Energy Lett.* **2017**, *2* (4), 876–881. https://doi.org/10.1021/acsenergylett.7b00135.

(40) Binninger, T.; Kowalski, P. M.; Eikerling, M. H. Oxygen Desorption – Critical Step for the Oxygen Evolution Reaction. *Current Opinion in Electrochemistry* **2023**, *42*, 101382. https://doi.org/10.1016/j.coelec.2023.101382.

(41) Binninger, T.; Doublet, M.-L. The Ir–OOOO–Ir Transition State and the Mechanism of the Oxygen Evolution Reaction on IrO$_2$ (110). *Energy Environ. Sci.* **2022**, *15* (6), 2519–2528. https://doi.org/10.1039/D2EE00158F.

(42) Ha, M.-A.; Larsen, R. E. Multiple Reaction Pathways for the Oxygen Evolution Reaction May Contribute to IrO$_2$ (110)'s High Activity. *J. Electrochem. Soc.* **2021**, *168* (2), 024506. https://doi.org/10.1149/1945-7111/abdeea.

(43) Govind Rajan, A.; Carter, E. A. Discovering Competing Electrocatalytic Mechanisms and Their Overpotentials: Automated Enumeration of Oxygen Evolution Pathways. *J. Phys. Chem. C* **2020**, *124* (45), 24883–24898. https://doi.org/10.1021/acs.jpcc.0c08120.

(44) Zhang, J.; Yang, H. B.; Zhou, D.; Liu, B. Adsorption Energy in Oxygen Electrocatalysis. *Chem. Rev.* **2022**, *122* (23), 17028–17072. https://doi.org/10.1021/acs.chemrev.1c01003.

(45) Wu, Y.; Ringe, S.; Wu, C.-L.; Chen, W.; Yang, A.; Chen, H.; Tang, M.; Zhou, G.; Hwang, H. Y.; Chan, K.; Cui, Y. A Two-Dimensional MoS$_2$ Catalysis Transistor by Solid-State Ion Gating Manipulation and Adjustment (SIGMA). *Nano Lett.* **2019**, *19* (10), 7293–7300. https://doi.org/10.1021/acs.nanolett.9b02888.

(46) Hansen, H. A.; Viswanathan, V.; Nørskov, J. K. Unifying Kinetic and Thermodynamic Analysis of 2 e$^-$ and 4 e$^-$ Reduction of Oxygen on Metal Surfaces. *J. Phys. Chem. C* **2014**, *118* (13), 6706–6718. https://doi.org/10.1021/jp4100608.

(47) Rebarchik, M.; Bhandari, S.; Kropp, T.; Mavrikakis, M. Insights into the Oxygen Evolution Reaction on Graphene-Based Single-Atom Catalysts from First-Principles-Informed Microkinetic Modeling. *ACS Catal.* **2023**, 5225–5235. https://doi.org/10.1021/acscatal.3c00474.

(48) Li, J.; Stenlid, J. H.; Ludwig, T.; Lamoureux, P. S.; Abild-Pedersen, F. Modeling Potential-Dependent Electrochemical Activation Barriers: Revisiting the Alkaline Hydrogen Evolution Reaction. *J. Am. Chem. Soc.* **2021**, *143* (46), 19341–19355. https://doi.org/10.1021/jacs.1c07276.

(49) Abidi, N.; Steinmann, S. N. How Are Transition States Modeled in Heterogeneous Electrocatalysis? *Current Opinion in Electrochemistry* **2022**, *33*, 100940.

https://doi.org/10.1016/j.coelec.2022.100940.

(50) Fang, Y.-H.; Liu, Z.-P. Tafel Kinetics of Electrocatalytic Reactions: From Experiment to First-Principles. *ACS Catal.* **2014**, *4* (12), 4364–4376. https://doi.org/10.1021/cs501312v.

(51) Resasco, J.; Abild-Pedersen, F.; Hahn, C.; Bao, Z.; Koper, M. T. M.; Jaramillo, T. F. Enhancing the Connection between Computation and Experiments in Electrocatalysis. *Nat Catal* **2022**, *5* (5), 374–381. https://doi.org/10.1038/s41929-022-00789-0.

(52) Antipin, D.; Risch, M. Calculation of the Tafel Slope and Reaction Order of the Oxygen Evolution Reaction between pH 12 and pH 14 for the Adsorbate Mechanism. *Electrochemical Science Adv* **2022**. https://doi.org/10.1002/elsa.202100213.

(53) Plaisance, C. P.; Beinlich, S. D.; Reuter, K. Kinetics-Based Computational Catalyst Design Strategy for the Oxygen Evolution Reaction on Transition-Metal Oxide Surfaces. *J. Phys. Chem. C* **2019**, *123* (13), 8287–8303. https://doi.org/10.1021/acs.jpcc.8b08549.

(54) Dickens, C. F.; Kirk, C.; Nørskov, J. K. Insights into the Electrochemical Oxygen Evolution Reaction with Ab Initio Calculations and Microkinetic Modeling: Beyond the Limiting Potential Volcano. *J. Phys. Chem. C* **2019**, *123* (31), 18960–18977. https://doi.org/10.1021/acs.jpcc.9b03830.

(55) Creazzo, F.; Luber, S. Water-Assisted Chemical Route Towards the Oxygen Evolution Reaction at the Hydrated (110) Ruthenium Oxide Surface: Heterogeneous Catalysis via DFT-MD and Metadynamics Simulations. *Chemistry A European J* **2021**, *27* (68), 17024–17037. https://doi.org/10.1002/chem.202102356.

(56) Duan, Z.; Xiao, P. Simulation of Potential-Dependent Activation Energies in Electrocatalysis: Mechanism of O–O Bond Formation on RuO_2. *J. Phys. Chem. C* **2021**, *125* (28), 15243–15250. https://doi.org/10.1021/acs.jpcc.1c02998.

(57) Nong, H. N.; Falling, L. J.; Bergmann, A.; Klingenhof, M.; Tran, H. P.; Spöri, C.; Mom, R.; Timoshenko, J.; Zichittella, G.; Knop-Gericke, A.; Piccinin, S.; Pérez-Ramírez, J.; Cuenya, B. R.; Schlögl, R.; Strasser, P.; Teschner, D.; Jones, T. E. Key Role of Chemistry versus Bias in Electrocatalytic Oxygen Evolution. *Nature* **2020**, *587* (7834), 408–413. https://doi.org/10.1038/s41586-020-2908-2.

(58) Patel, A. M.; Vijay, S.; Kastlunger, G.; Nørskov, J. K.; Chan, K. Generalizable Trends in

(59) Ping, Y.; Nielsen, R. J.; Goddard, W. A. The Reaction Mechanism with Free Energy Barriers at Constant Potentials for the Oxygen Evolution Reaction at the IrO_2 (110) Surface. *J. Am. Chem. Soc.* **2017**, *139* (1), 149–155. https://doi.org/10.1021/jacs.6b07557.

(60) Tripković, V.; Skúlason, E.; Siahrostami, S.; Nørskov, J. K.; Rossmeisl, J. The Oxygen Reduction Reaction Mechanism on Pt (111) from Density Functional Theory Calculations. *Electrochim. Acta* **2010**, *55* (27), 7975–7981. https://doi.org/10.1016/j.electacta.2010.02.056.

(61) Xiao, H.; Shin, H.; Goddard, W. A. Synergy between Fe and Ni in the Optimal Performance of (Ni,Fe)OOH Catalysts for the Oxygen Evolution Reaction. *Proc. Natl. Acad. Sci. U.S.A.* **2018**, *115* (23), 5872–5877. https://doi.org/10.1073/pnas.1722034115.

(62) Zagalskaya, A.; Evazzade, I.; Alexandrov, V. *Ab Initio* Thermodynamics and Kinetics of the Lattice Oxygen Evolution Reaction in Iridium Oxides. *ACS Energy Lett.* **2021**, *6* (3), 1124–1133. https://doi.org/10.1021/acsenergylett.1c00234.

(63) Baz, A.; Dix, S. T.; Holewinski, A.; Linic, S. Microkinetic Modeling in Electrocatalysis: Applications, Limitations, and Recommendations for Reliable Mechanistic Insights. *Journal of Catalysis* **2021**, *404*, 864–872. https://doi.org/10.1016/j.jcat.2021.08.043.

(64) Motagamwala, A. H.; Dumesic, J. A. Microkinetic Modeling: A Tool for Rational Catalyst Design. *Chem. Rev.* **2021**, *121* (2), 1049–1076. https://doi.org/10.1021/acs.chemrev.0c00394.

(65) Bezanson, J.; Edelman, A.; Karpinski, S.; Shah, V. B. Julia: A Fresh Approach to Numerical Computing. *SIAM Review* **2017**, *59* (1), 65–98. https://doi.org/doi/10.1137/141000671.

(66) Rackauckas, C.; Nie, Q. DifferentialEquations.Jl – A Performant and Feature-Rich Ecosystem for Solving Differential Equations in Julia. *JORS* **2017**, *5* (1), 15. https://doi.org/10.5334/jors.151.

(67) Wei, C.; Xu, Z. J. The Comprehensive Understanding of 10 mA Cm_{geo}^{-2} as an Evaluation Parameter for Electrochemical Water Splitting. *Small Methods* **2018**, *2* (11), 1800168. https://doi.org/10.1002/smtd.201800168.

(68) Danilovic, N.; Subbaraman, R.; Chang, K.-C.; Chang, S. H.; Kang, Y. J.; Snyder, J.; Paulikas, A. P.; Strmcnik, D.; Kim, Y.-T.; Myers, D.; Stamenkovic, V. R.; Markovic, N. M. Activity–

Stability Trends for the Oxygen Evolution Reaction on Monometallic Oxides in Acidic Environments. *J. Phys. Chem. Lett.* **2014**, *5* (14), 2474–2478. https://doi.org/10.1021/jz501061n.

(69) Shi, Z.; Wang, X.; Ge, J.; Liu, C.; Xing, W. Fundamental Understanding of the Acidic Oxygen Evolution Reaction: Mechanism Study and State-of-the-Art Catalysts. *Nanoscale* **2020**, *12* (25), 13249–13275. https://doi.org/10.1039/D0NR02410D.

(70) Yu, J.; Garcés-Pineda, F. A.; González-Cobos, J.; Peña-Díaz, M.; Rogero, C.; Giménez, S.; Spadaro, M. C.; Arbiol, J.; Barja, S.; Galán-Mascarós, J. R. Sustainable Oxygen Evolution Electrocatalysis in Aqueous 1 M H2SO4 with Earth Abundant Nanostructured Co3O4. *Nat Commun* **2022**, *13* (1), 4341. https://doi.org/10.1038/s41467-022-32024-6.

(71) Yu, J.; Giancola, S.; Khezri, B.; Nieto-Castro, D.; Redondo, J.; Schiller, F.; Barja, S.; Spadaro, M. C.; Arbiol, J.; Garcés-Pineda, F. A.; Galán-Mascarós, J. R. A Survey of Earth-Abundant Metal Oxides as Oxygen Evolution Electrocatalysts in Acidic Media (pH < 1). *EES. Catal.* **2023**, *1* (5), 765–773. https://doi.org/10.1039/D3EY00101F.

(72) Matsumoto, Y.; Sato, E. Electrocatalytic Properties of Transition Metal Oxides for Oxygen Evolution Reaction. *Mater. Chem. Phys.* **1986**, *14* (5), 397–426. https://doi.org/10.1016/0254-0584(86)90045-3.

(73) Exner, K. S.; Over, H. Beyond the Rate-Determining Step in the Oxygen Evolution Reaction over a Single-Crystalline IrO2 (110) Model Electrode: Kinetic Scaling Relations. *ACS Catal.* **2019**, *9* (8), 6755–6765. https://doi.org/10.1021/acscatal.9b01564.

(74) Rao, R. R.; Kolb, M. J.; Halck, N. B.; Pedersen, A. F.; Mehta, A.; You, H.; Stoerzinger, K. A.; Feng, Z.; Hansen, H. A.; Zhou, H.; Giordano, L.; Rossmeisl, J.; Vegge, T.; Chorkendorff, I.; Stephens, I. E. L.; Shao-Horn, Y. Towards Identifying the Active Sites on RuO2 (110) in Catalyzing Oxygen Evolution. *Energy Environ. Sci.* **2017**, *10* (12), 2626–2637. https://doi.org/10.1039/C7EE02307C.

(75) Rao, R. R.; Kolb, M. J.; Giordano, L.; Pedersen, A. F.; Katayama, Y.; Hwang, J.; Mehta, A.; You, H.; Lunger, J. R.; Zhou, H.; Halck, N. B.; Vegge, T.; Chorkendorff, I.; Stephens, I. E. L.; Shao-Horn, Y. Operando Identification of Site-Dependent Water Oxidation Activity on Ruthenium Dioxide Single-Crystal Surfaces. *Nat Catal* **2020**, *3* (6), 516–525.

https://doi.org/10.1038/s41929-020-0457-6.

(76) Gopeesingh, J.; Ardagh, M. A.; Shetty, M.; Burke, S. T.; Dauenhauer, P. J.; Abdelrahman, O. A. Resonance-Promoted Formic Acid Oxidation via Dynamic Electrocatalytic Modulation. *ACS Catal.* **2020**, *10* (17), 9932–9942. https://doi.org/10.1021/acscatal.0c02201.

(77) Román, A. M.; Spivey, T. D.; Medlin, J. W.; Holewinski, A. Accelerating Electro-Oxidation Turnover Rates via Potential-Modulated Stimulation of Electrocatalytic Activity. *Ind. Eng. Chem. Res.* **2020**, *59* (45), 19999–20010. https://doi.org/10.1021/acs.iecr.0c04414.

(78) Bui, J. C.; Kim, C.; Weber, A. Z.; Bell, A. T. Dynamic Boundary Layer Simulation of Pulsed CO₂ Electrolysis on a Copper Catalyst. *ACS Energy Lett.* **2021**, 1181–1188. https://doi.org/10.1021/acsenergylett.1c00364.

(79) Kim, C.; Weng, L.-C.; Bell, A. T. Impact of Pulsed Electrochemical Reduction of CO₂ on the Formation of C₂₊ Products over Cu. *ACS Catal.* **2020**, *10* (21), 12403–12413. https://doi.org/10.1021/acscatal.0c02915.

(80) Lim, C. W.; Hülsey, M. J.; Yan, N. Non-Faradaic Promotion of Ethylene Hydrogenation under Oscillating Potentials. *JACS Au* **2021**, *1* (5), 536–542. https://doi.org/10.1021/jacsau.1c00044.

(81) Murphy, M.; Gathmann, S. R.; Bartel, C. J.; Abdelrahman, O. A.; Dauenhauer, P. *Catalytic Resonance Theory: Circumfluence of Programmable Catalytic Loops*; preprint; Chemistry, 2023. https://doi.org/10.26434/chemrxiv-2023-xmb84.

(82) Astumian, R. D.; Robertson, B. Imposed Oscillations of Kinetic Barriers Can Cause an Enzyme to Drive a Chemical Reaction Away from Equilibrium. *J. Am. Chem. Soc.* **1993**, *115* (24), 11063–11068. https://doi.org/10.1021/ja00077a001.

(83) Astumian, R. D. Kinetic Asymmetry Allows Macromolecular Catalysts to Drive an Information Ratchet. *Nat Commun* **2019**, *10* (1), 3837. https://doi.org/10.1038/s41467-019-11402-7.

(84) Amano, S.; Esposito, M.; Kreidt, E.; Leigh, D. A.; Penocchio, E.; Roberts, B. M. W. Using Catalysis to Drive Chemistry Away from Equilibrium: Relating Kinetic Asymmetry, Power Strokes, and the Curtin–Hammett Principle in Brownian Ratchets. *J. Am. Chem. Soc.* **2022**, *144* (44), 20153–20164. https://doi.org/10.1021/jacs.2c08723.

(85) Jerkiewicz, G. Standard and Reversible Hydrogen

Electrodes: Theory, Design, Operation, and Applications. *ACS Catal.* **2020**, *10* (15), 8409–8417. https://doi.org/10.1021/acscatal.0c02046.

(86) Govind Rajan, A.; Carter, E. A. Microkinetic Model for pH- and Potential-Dependent Oxygen Evolution during Water Splitting on Fe-Doped β-NiOOH. *Energy Environ. Sci.* **2020**, *13* (12), 4962–4976. https://doi.org/10.1039/D0EE02292F.

(87) Nørskov, J. K.; Rossmeisl, J.; Logadottir, A.; Lindqvist, L.; Kitchin, J. R.; Bligaard, T.; Jónsson, H. Origin of the Overpotential for Oxygen Reduction at a Fuel-Cell Cathode. *J. Phys. Chem. B* **2004**, *108* (46), 17886–17892. https://doi.org/10.1021/jp047349j.

(88) Warburton, R. E.; Soudackov, A. V.; Hammes-Schiffer, S. Theoretical Modeling of Electrochemical Proton-Coupled Electron Transfer. *Chem. Rev.* **2022**, *122* (12), 10599–10650. https://doi.org/10.1021/acs.chemrev.1c00929.

(89) Hunter, J. D. Matplotlib: A 2D Graphics Environment. *Comput. Sci. Eng.* **2007**, *9* (3), 90–95. https://doi.org/10.1109/MCSE.2007.55.

(90) Hairer, E.; Wanner, G. Stiff Differential Equations Solved by Radau Methods. *Journal of Computational and Applied Mathematics* **1999**, *111*, 93–111.

(91) Campbell, C. T. The Degree of Rate Control: A Powerful Tool for Catalysis Research. *ACS Catal.* **2017**, *7* (4), 2770–2779. https://doi.org/10.1021/acscatal.7b00115.

(92) Yang, Y.; Achar, S. K.; Kitchin, J. R. Evaluation of the Degree of Rate Control via Automatic Differentiation. *AIChE Journal* **2022**, *68* (6). https://doi.org/10.1002/aic.17653.

(93) Revels, J.; Lubin, M.; Papamarkou, T. Forward-Mode Automatic Differentiation in Julia. arXiv July 26, 2016. http://arxiv.org/abs/1607.07892 (accessed 2023-12-10).

(94) Rackauckas, C.; Ma, Y.; Martensen, J.; Warner, C.; Zubov, K.; Supekar, R.; Skinner, D.; Ramadhan, A.; Edelman, A. Universal Differential Equations for Scientific Machine Learning. arXiv November 2, 2021. http://arxiv.org/abs/2001.04385 (accessed 2023-12-10).

(95) Akhade, S. A.; Nidzyn, R. M.; Rostamikia, G.; Janik, M. J. Using Brønsted-Evans-Polanyi Relations to Predict Electrode Potential-Dependent Activation Energies. *Catalysis Today* **2018**, *312*, 82–91. https://doi.org/10.1016/j.cattod.2018.03.048.

(96) Curutchet, A.; Colinet, P.; Michel, C.; Steinmann, S. N.; Le Bahers, T. Two-Sites Are Better than One: Revisiting the OER Mechanism on CoOOH by DFT with Electrode Polarization. *Phys. Chem. Chem. Phys.* **2020**, *22* (13), 7031–7038. https://doi.org/10.1039/D0CP00281J.

(97) Plaisance, C. P.; van Santen, R. A. Structure Sensitivity of the Oxygen Evolution Reaction Catalyzed by Cobalt(II,III) Oxide. *J. Am. Chem. Soc.* **2015**, *137* (46), 14660–14672. https://doi.org/10.1021/jacs.5b07779.

(98) Godínez-Salomón, F.; Albiter, L.; Alia, S. M.; Pivovar, B. S.; Camacho-Forero, L. E.; Balbuena, P. B.; Mendoza-Cruz, R.; Arellano-Jimenez, M. J.; Rhodes, C. P. Self-Supported Hydrous Iridium–Nickel Oxide Two-Dimensional Nanoframes for High Activity Oxygen Evolution Electrocatalysts. *ACS Catal.* **2018**, *8* (11), 10498–10520. https://doi.org/10.1021/acscatal.8b02171.

(99) Camacho-Forero, L. E.; Godínez-Salomón, F.; Ramos-Sánchez, G.; Rhodes, C. P.; Balbuena, P. B. Theoretical and Experimental Study of the Effects of Cobalt and Nickel Doping within IrO_2 on the Acidic Oxygen Evolution Reaction. *Journal of Catalysis* **2022**, *408*, 64–80. https://doi.org/10.1016/j.jcat.2022.02.016.

(100) Geppert, J.; Röse, P.; Pauer, S.; Krewer, U. Microkinetic Barriers of the Oxygen Evolution on the Oxides of Iridium, Ruthenium and Their Binary Mixtures. *ChemElectroChem* **2022**, *9* (20). https://doi.org/10.1002/celc.202200481.

(101) Geppert, J.; Röse, P.; Czioska, S.; Escalera-López, D.; Boubnov, A.; Saraçi, E.; Cherevko, S.; Grunwaldt, J.-D.; Krewer, U. Microkinetic Analysis of the Oxygen Evolution Performance at Different Stages of Iridium Oxide Degradation. *J. Am. Chem. Soc.* **2022**, *144* (29), 13205–13217. https://doi.org/10.1021/jacs.2c03561.

(102) Schuler, T.; Kimura, T.; Schmidt, T. J.; Büchi, F. N. Towards a Generic Understanding of Oxygen Evolution Reaction Kinetics in Polymer Electrolyte Water Electrolysis. *Energy Environ. Sci.* **2020**, *13* (7), 2153–2166. https://doi.org/10.1039/D0EE00673D.

(103) Fang, Y.-H.; Liu, Z.-P. Mechanism and Tafel Lines of Electro-Oxidation of Water to Oxygen on RuO_2 (110). *J. Am. Chem. Soc.* **2010**, *132* (51), 18214–18222. https://doi.org/10.1021/ja1069272.

(104) Wen, Y.; Liu, C.; Huang, R.; Zhang, H.; Li, X.; García de Arquer, F. P.; Liu, Z.; Li, Y.; Zhang, B. Introducing Brønsted Acid Sites to Accelerate the Bridging-Oxygen-Assisted Deprotonation in Acidic Water Oxidation. *Nat Commun* **2022**, *13* (1), 4871. https://doi.org/10.1038/s41467-022-

---

32581-w.

(105) Tayyebi, E.; Höskuldsson, Á. B.; Wark, A.; Atrak, N.; Comer, B. M.; Medford, A. J.; Skúlason, E. Perspectives on the Competition between the Electrochemical Water and N2 Oxidation on a TiO2 (110) Electrode. *J. Phys. Chem. Lett.* **2022**, *13* (26), 6123–6129. https://doi.org/10.1021/acs.jpclett.2c00769.

(106) Stecher, T.; Reuter, K.; Oberhofer, H. First-Principles Free-Energy Barriers for Photoelectrochemical Surface Reactions: Proton Abstraction at TiO2 (110). *Phys. Rev. Lett.* **2016**, *117* (27), 276001. https://doi.org/10.1103/PhysRevLett.117.276001.

(107) Tao, H. B.; Zhang, J.; Chen, J.; Zhang, L.; Xu, Y.; Chen, J. G.; Liu, B. Revealing Energetics of Surface Oxygen Redox from Kinetic Fingerprint in Oxygen Electrocatalysis. *J. Am. Chem. Soc.* **2019**, *141* (35), 13803–13811. https://doi.org/10.1021/jacs.9b01834.

(108) Jinnouchi, R.; Kodama, K.; Hatanaka, T.; Morimoto, Y. First Principles Based Mean Field Model for Oxygen Reduction Reaction. *Phys. Chem. Chem. Phys.* **2011**, *13* (47), 21070. https://doi.org/10.1039/c1cp21349k.

(109) Duan, Z.; Wang, G. A First Principles Study of Oxygen Reduction Reaction on a Pt (111) Surface Modified by a Subsurface Transition Metal M (M = Ni, Co, or Fe). *Phys. Chem. Chem. Phys.* **2011**, *13* (45), 20178. https://doi.org/10.1039/c1cp21687b.

(110) Huang, J.; Zhang, J.; Eikerling, M. Unifying Theoretical Framework for Deciphering the Oxygen Reduction Reaction on Platinum. *Phys. Chem. Chem. Phys.* **2018**, *20* (17), 11776–11786. https://doi.org/10.1039/C8CP01315B.

(111) Wei, G.-F.; Fang, Y.-H.; Liu, Z.-P. First Principles Tafel Kinetics for Resolving Key Parameters in Optimizing Oxygen Electrocatalytic Reduction Catalyst. *J. Phys. Chem. C* **2012**, *116* (23), 12696–12705. https://doi.org/10.1021/jp3034616.

(112) Roudgar, A.; Eikerling, M.; van Santen, R. *Ab Initio* Study of Oxygen Reduction Mechanism at Pt4 Cluster. *Phys. Chem. Chem. Phys.* **2010**, *12* (3), 614–620. https://doi.org/10.1039/B914570B.

(113) Ford, D. C.; Nilekar, A. U.; Xu, Y.; Mavrikakis, M. Partial and Complete Reduction of O2 by Hydrogen on Transition Metal Surfaces. *Surface Science* **2010**, *604* (19–20), 1565–1575. https://doi.org/10.1016/j.susc.2010.05.026.

(114) Du, X.; Liu, G.; Luo, Y.; Li, J.; Ricardez-Sandoval, L. Theoretical Insights into the Oxygen Reduction Reaction on PtCu (111): Effects of Surface Defect and Acidic Solvent. *Applied Surface Science* **2021**, *570*, 151195. https://doi.org/10.1016/j.apsusc.2021.151195.

(115) Fajín, J. L. C.; Cordeiro, M. N. D. S.; Illas, F.; Gomes, J. R. B. Descriptors Controlling the Catalytic Activity of Metallic Surfaces toward Water Splitting. *Journal of Catalysis* **2010**, *276* (1), 92–100. https://doi.org/10.1016/j.jcat.2010.09.007.

(116) Yatom, N.; Neufeld, O.; Caspary Toroker, M. Toward Settling the Debate on the Role of Fe2O3 Surface States for Water Splitting. *J. Phys. Chem. C* **2015**, *119* (44), 24789–24795. https://doi.org/10.1021/acs.jpcc.5b06128.

(117) Meng, C.; Gao, Y.-F.; Chen, X.-M.; Li, Y.-X.; Lin, M.-C.; Zhou, Y. Activating Inert ZnO by Surface Cobalt Doping for Efficient Water Oxidation in Neutral Media. **2019**.